

# High-temperature nitrous oxide absorption sensor for shock tube kinetics near 4.4 µm

Benjamin R. Steavenson\*, Laura Munera\*, Matthew B. Johnson\*, Aubrey M. Fuchs<sup>†</sup>, and Daniel I. Pineda<sup>‡</sup> The University of Texas at San Antonio (UTSA), San Antonio, Texas, 78249, USA

Here we describe the development of a mid-infrared laser absorption spectroscopy sensing method for the time-resolved thermochemical analysis of nitrous oxide ( $N_2O$ ) in high-enthalpy, combustion-relevant environments. This was accomplished by scanning the wavelength of a quantum cascade laser across multiple R-branch spectral features in the  $\nu_3$  rovibrational fundamental band between 2257 and 2265 cm $^{-1}$ . Four total rovibrational transitions are spectrally resolved over a  $\sim 1.6~{\rm cm}^{-1}$  domain using a 10 kHz sawtooth waveform function supplied to the quantum cascade laser, yielding time-resolved temperature and concentration measurements that are independent of mixture composition. Additionally, we demonstrate a measurement approach with increased robustness against signal noise for a reacting mixture containing  $N_2O$  in high-dilution conditions in argon gas. This measurement approach is demonstrated across a range of high temperatures (900–1700 K) behind reflected shock waves at The University of Texas at San Antonio (UTSA) High-Enthalpy Shock Tube (HEST) facility, and applications to research and development efforts of both "green" propellant architectures as well as nitrogen-based hydrogen-carrier fuels are briefly discussed.

## I. Nomenclature

 $\alpha$  = absorbance

 $\nu$  = spectral frequency

 $v_0$  = spectral transition linecenter frequency

 $\varphi$  = spectral lineshape  $\Delta v_D$  = Doppler width  $\Delta v_C$  = collisional width

P = pressure

X = species mole fraction

S = linestrength T = temperature L = path length A = absorption area M = molecular weight

LAS = laser absorption spectroscopy
QCL = quantum cascade laser
HEST = high-enthalpy shock tube

## **II. Introduction**

Current understanding of the chemical kinetic and detonative behavior of both established space-storable liquid propellants—and their potential replacements—is immature relative to that of  $H_2$ ,  $CH_4$ , and  $C_2H_4$ , or even hydrocarbon fuels used for non-space transportation. Moreover, as terrestrial transportation and power generation sectors move to an increasingly carbon-constrained future, near-zero carbon energy conversion through the use of

<sup>\*</sup>Graduate Research Assistant, Dept. of Mechanical Engineering, 1 UTSA Circle, AIAA Student Member.

<sup>&</sup>lt;sup>†</sup>Undergraduate Research Assistant, Dept. of Mechanical Engineering, 1 UTSA Circle, AIAA Student Member.

<sup>&</sup>lt;sup>‡</sup>Assistant Professor, Dept. of Mechanical Engineering, 1 UTSA Circle, AIAA Member.

nitrogen-based hydrogen-carrier fuels (e.g.,  $NH_3$ ) will become increasingly important. However, reaction of these propellants is not well-characterized—especially in non-uniform flows relevant to combustion devices—primarily due to immature diagnostic capabilities. The objective of this work is to develop a gas-composition-independent measurement technique to quantify  $N_2O$  mole fraction and temperature as it thermally reacts, developing time-histories for the comparison with published chemical kinetic models.

Multiple species-specific, temporally-resolved mole fraction studies involving the oxidation of  $NH_3$  and its intermediate  $N_2O$  have been conducted in recent years. Several studies using fixed-wavelength laser absorption spectroscopy (LAS) were performed by Mulvihill et al., investigating  $N_2O$  sensing and thermal decomposition [1] at high temperatures. Additionally, a similar fixed-wavelength approach to measure  $N_2O$  mole fraction behind reflected shock waves containing  $NH_3$  at elevated temperatures was also performed [3]. In this study, we describe the development of a mid-infrared (mid-IR) laser absorption sensor concept based on scanned-wavelength techniques which can quantitatively measure  $N_2O$  in high-enthalpy, combustion-relevant environments. We describe the theory of LAS underlying the sensing technique, detail our wavelength selection, and demonstrate the strategy over a range of temperatures (900–1700 K) behind reflected shock waves using UTSA's optically-accessible HEST facility. This range of temperatures is chosen for its relevance to emerging "green" propellant architectures and nitrogen-based hydrogen-carrier fuel systems associated with space transportation and energy production, respectively. Lastly, we use the developed technique to provide transient measurements of thermally reacting  $N_2O$  in the UTSA HEST facility, highlighting potential opportunities for sensing applications in the aerospace, transportation, and power generation sectors.

## III. Background

In this section, we provide background information on the laser absorption spectroscopy techniques specific to our work developing an  $N_2O$  sensor, while the theory of shock tube operation can be found in any compressible flow text  $\square$  or in our previous work detailing the design of our shock tube facility  $\square$ .

#### A. Laser absorption spectroscopy and two-line thermometry

Laser absorption spectroscopy leverages the resonance of monochromatic collimated laser light energy with the discrete energy modes of gas molecules and atoms (arising from quantum mechanics) to discern thermochemical properties of flow fields using light absorption. The details of laser absorption spectroscopy are described in the literature and in previous work [6, 7]; however, we briefly review the fundamentals of LAS to assist the reader with the measurements described in this paper.

The Beer-Lambert law, shown in Eq. (1), describes the relationship between spectral and thermodynamic variables, as well as incident and transmitted laser light intensity  $I_0$  and  $I_t$ . By integrating Eq. (1) with respect to frequency  $\nu$  [cm<sup>-1</sup>], absorbance area  $A_j$  [cm<sup>-1</sup>] can be determined from spectrally-resolved absorbance  $\alpha(\nu)$  [unitless], shown below in Eq. (2), being only a function of the thermophysical variables pressure P [atm], absorbing species mole fraction X, transition linestrength  $S_j(T)$  [cm<sup>-2</sup>/atm], and optical path-length L [cm] (6), which is well-known in this study to be 7.77 cm for the UTSA HEST facility.

$$\alpha(\nu) = -\ln\left(\frac{I_t}{I_0}\right) = PXS_j(T)L\varphi_j(\nu) \tag{1}$$

$$A_{j} = \int_{-\infty}^{\infty} \alpha(\nu) d\nu = PXS_{j}(T)L$$
 (2)

To measure one or more spectral absorption features (in this work, rovibrational transitions), laser light is scanned across a range of wavelengths while passing through a test gas and into a photovoltaic detector, on which laser intensity is recorded. Upon absorption by a rovibrational transition, the transmitted laser light upon the detector is reduced.

To interpret the measured absorption data, a Voigt lineshape model (a convolution of a Gaussian and Lorentzian profile) can be fit to measured  $\alpha(\nu)$  using non-linear regression [8]. As part of the non-linear fitting routine, the spectral lineshape function at the linecenter  $\varphi_j(\nu_{0,j})$  [unitless] is numerically evaluated using Eqs. (3) and (4).

$$\varphi_j(\nu_{0,j}) = \frac{2}{\Delta\nu_{D,j}} \sqrt{\frac{\ln 2}{\pi}} \exp a^2 [1 - \operatorname{erf}(a)]$$
(3)

where

$$a = \frac{\sqrt{\ln 2\Delta \nu_{c,j}}}{\Delta \nu_{D,j}} \tag{4}$$

The Doppler and collisional widths,  $\Delta v_{D,j}$  and  $\Delta v_{c,j}$  [cm<sup>-1</sup>], represent the uncertainty in spectral feature full-width half-maximum (FWHM) due to the effects of temperature and pressure. Doppler width, being a function of both temperature T [K] and molecular weight of the absorbing species M [g/mole], is shown in Eq. (5). Collisional width, being a function of pressure P, mole fraction X, and has unique broadening behavior for every molecular collision partner Y.

$$\Delta v_{D,j} = v_{0,j} (7.1629 \times 10^{-7}) \left(\frac{T}{M}\right)^{1/2}$$
 (5)

$$\Delta \nu_{c,j} = P \sum_{\mathbf{Y}} (X_{\mathbf{Y}} 2 \gamma_{\text{abs-Y},j}(T)) \tag{6}$$

where  $2\gamma(T)_{\text{abs-Y},j}$  [cm<sup>-1</sup>/atm] is the temperature dependant broadening coefficient between collision partner Y and the absorbing species, commonly modeled by a power law where N is a temperature-dependent exponent.

$$2\gamma(T)_{\text{abs-Y},j} = 2\gamma(T_0)_{\text{abs-Y},j} \left(\frac{T_0}{T}\right)^{N_j} \tag{7}$$

After spectrally fitting to this Voigt lineshape model (either by performing a non-linear least-squares fit of either the spectral parameters  $\Delta v_{c,j}$ ,  $\Delta v_{D,j}$ ,  $A_j$ , and  $v_{0,j}$ ; or—if  $\varphi_j(T,P,X,\nu)$  is well-characterized—of the underlying thermodynamic state variables X, P, and T),  $A_j$  can be numerically evaluated, assisting in the determination of thermodynamic state variables T and X as shown in Eq. [2] assuming that L is known from the experimental geometry and P is known independently. For multiple absorption features j, multiple  $A_j$  can be determined. The ratio of two absorption areas or integrated spectral absorption coefficients reduces to a ratio, R, of  $S_j(T)$ , being a function of T only, is shown in Eq. [8]

$$R = \frac{A_1}{A_2} = \frac{S_1(T)}{S_2(T)} = f(T) \tag{8}$$

Because  $S_j(T)$  is a feature- or transition-specific spectral property, calculable from values readily available in the HITEMP and HITRAN databases  $[9, \overline{10}]$ , it is possible to infer T with the simultaneous measurement of two or more spectral absorption features. With T determined,  $S_j(T)$  can be evaluated and X can be calculated using Eq. [9].

$$X = \frac{A_j}{PS_j(T)L} \tag{9}$$

### **B.** Boltzmann regression

If multiple absorption features are simultaneously recorded (generally more than two), a multi-line Boltzmann regression of rovibrational state population fractions can be used to determine temperature and species mole fraction. More details regarding this technique are described in the literature as well as in our previous work targeting N<sub>2</sub>O near 4.4 µm [T], however, we review some details here for reader convenience. The linestrength of a single spectral transition j, shown in Eq. (T], is a function of temperature, the partition function variation multiplied by a stimulated emission factor,  $z(T, \bar{v_j})$  [unitless], the lower state energy of the transition,  $E''_j$  [cm<sup>-1</sup>], and a reference temperature usually taken at  $T_0 = 296$  K (T).

$$S_j(T) = S_j^0 z(T, \bar{\nu_j}) \left(\frac{T_0}{T}\right) \exp\left[-\frac{hcE_j^{\prime\prime}}{k_B} \left(\frac{1}{T} - \frac{1}{T_0}\right)\right]$$

$$\tag{10}$$

where the linestrength evaluated at the reference temperature is noted as  $S_j^0 = S_j(T_0)$  and  $z(T, \bar{v_j})$ , is a function of the partition function,  $\mathcal{Z}(T)$  [unitless], and the linecenter  $v_j$  [cm<sup>-1</sup>]. Combining Eq. (2) with Eq. (10) and linearizing:

$$\ln\left[\frac{A_j}{PS_j^0L}\right] = \ln\left[Xz(T)\left(\frac{T_0}{T}\right)\right] + E_j^{"}\left[\frac{hc}{k_B}\left(\frac{1}{T_0} - \frac{1}{T}\right)\right] \tag{11}$$

This linear relationship, which is of the form y = ax + b, is a direct representation of the Boltzmann distribution of state populations [12].

Thus,  $\frac{A_j}{PS_j^0L}$  is related to the degree with which the lower state of the transition j at temperature T is populated relative to the population at the reference temperature  $T_0$ , illustrated below in Fig.  $\boxed{1}$ 

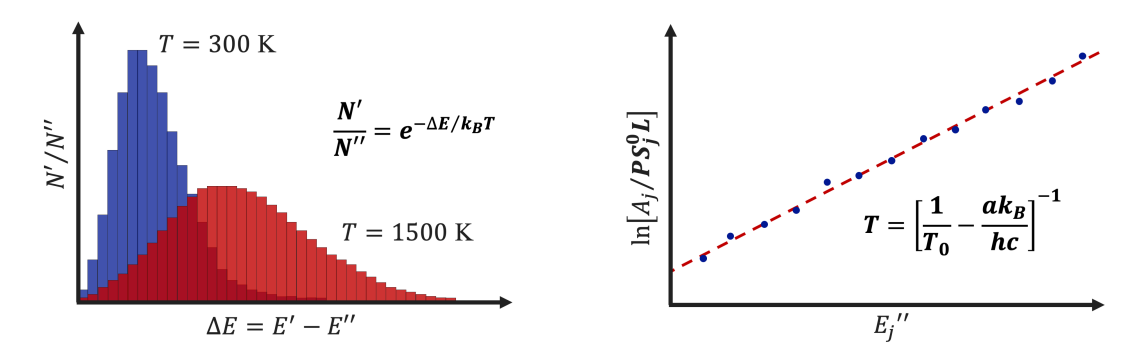


Fig. 1 Left: Boltzmann distribution of populated energy states at two representative temperatures. Here, the double prime indicates the lower state while the single prime indicates the upper state. Right: Linearization of Eq. (11) for multiple spectral absorption features j, illustrating the relationship between the regressions slope, a [cm] with temperature, T.

## IV. Method

### A. Wavelength selection

Three primary criteria; absorbance strength, spectral isolation, and temperature sensitivity are considered when selecting spectral features for temperature and mole fraction measurements [13]. Absorbance strength is a measure of the intensity of a spectral absorption feature at a given spectral frequency and is tabulated as linestrength S at a reference temperature (commonly 296 K) in spectral databases (e.g., HITRAN, HITEMP). Spectral isolation describes how well-separated a spectral absorption feature of interest is from other spectral features that could be present in the targeted range of spectral frequencies. Ideally, one or more spectral absorption features will be present in a single laser scan along with a region of zero or near-zero absorbance for baseline correction of any beam-steering behavior encountered in the flow [14]. Temperature sensitivity is a measure of how a spectral absorption feature develops/changes shape with changes in temperature and is critical for robust temperature measurements. To perform two-line thermometry, two spectral absorption features with relatively large differences in lower state energy, E" should be used, a metric that is tabulated, like linestrength, in spectral databases. However, if features with large differences in lower state energy are not available, temperature measurements can still be obtained via Boltzmann regression providing a sufficient number of spectral absorption features are used.

A Quantum Cascade Laser (QCL, Alpes Lasers), centered at 4.42  $\mu$ m and having a scanning range from 2256 cm<sup>-1</sup> to 2268 cm<sup>-1</sup>, was used to target the  $v_3$  asymmetric stretch band of N<sub>2</sub>O. Figure 2 shows the simulated absorbance (red) and linestrengths (blue) for N<sub>2</sub>O in this spectral frequency range and for the path length in the UTSA HEST facility (L = 7.77 cm). Additionally, the simulated absorbance of H<sub>2</sub>O and CO<sub>2</sub> are shown, being a common interferer and present in the ambient laboratory atmosphere, respectively.

To the left, near 2259 cm<sup>-1</sup>, a R-branch bandhead can be seen. Although these lines offer high contrast in lower state energy, they are not well isolated, leading to no near non-absorbing regions. Due to this, spectral absorption lines located to the right of the bandhead were targeted in these experiments. The lines to the right of the bandhead all have relatively high absorbance strength and are spectrally isolated from one another. However, they also all have similar lower state energies. To counteract this, the large scan depth of the QCL at a scan rate of 10 kHz was leveraged to resolve 4 spectral absorption features (labeled) and temperature and mole fraction were inferred via Boltzmann regression.

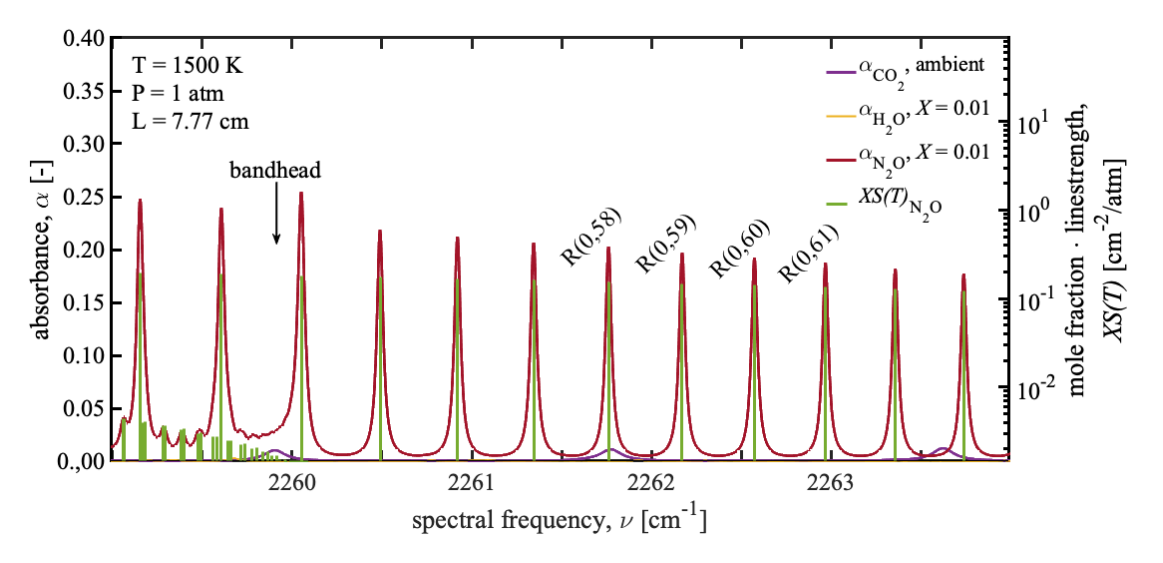


Fig. 2  $N_2O$  spectral features and  $N_2O$ ,  $H_2O$ , and ambient  $CO_2$  simulated absorbance at and pressures relevant to combustion.

#### **B.** Optical setup

To obtain measurements of N<sub>2</sub>O mole fraction and temperature, the QCL was used as a light source, and the beam was passed through optical ports in the test section of the UTSA HEST, as shown in Fig. 3. The injection current of the laser was modulated at 10 kHz using a function generator (Stanford Research Systems DS345), allowing the R(0,58–61) spectral features to be fully resolved. To account for scan-to-scan variability in laser scan depth, the beam was directed through a non-polarizing beam splitter before passing through the optical section of the HEST, with the split portion of the beam passing through a germanium (Ge) etalon crystal and onto a photovoltaic detector (Vigo Photonics PVI-4TE-6-1), allowing for the scan-by-scan conversion from the time to spectral frequency domain of the measured laser light intensity. The HEST test section contains six, 1/2-inch wedged sapphire windows mounted 2 cm from the end wall and a inner diameter of 7.77 cm [5], with an end-wall mounted dynamic pressure transducer connected to a charge amplifier. After passing through the HEST, the beam was passed through a focusing lens and iris, both increasing signal-to-noise ratio (SNR), and onto a second photovoltaic detector. Laser intensities were recorded in volts [V] at a sample rate of 40 Ms/s/channel using an external oscilloscope (PicoScope 4000). This resulted in 10 ms measurements during which the laser was scanned 100 times. A schematic of the optical setup is shown in Fig. 3. Here, a representative temporally-resolved measurement of laser intensity and dynamic pressure as the shock wave is reflected off of the end wall of the test section are shown below the optical arrangement.

## C. Shock tube experiments

Shock tube experiments were performed utilizing the UTSA HEST facility with nitrogen ( $N_2$ ) as a driver gas. Test gas mixtures of  $X \approx 0.02$  mole fraction  $N_2O$  in an Ar bath gas were barometrically prepared based on partial pressures measured with a 1000 Torr capacitance manometer (MKS Baratron 627B). Driven pressure ( $P_1$ ), polycarbonate diaphragm thickness, and driver (diaphragm burst) pressure ( $P_4$ ) were varied such that reflected shock wave temperatures ( $T_5$ ) ranged from approximately 900–1700 K. Prior to each experiment, the shock tube was vacuumed to under 20 mTorr, measured with a 1 Torr capacitance manometer (MKS Baratron 627B). Pre-shock pressures  $P_1$  in the driven section were measured using the aforementioned 1000 Torr capacitance manometer while driver pressure was monitored with a 250 psi pressure transducer (Setra 225). Incident shock wave speed was determined via linear regression of temporally-resolved voltage peaks from piezoelectric pins (Dynasen, Inc. CA-1135) spaced at precisely-known distances along the driver section of the tube, as described in previous work [5]. NASA's Chemical Equilibrium with Applications (CEA) [15] was used to determine theoretical  $T_5$  and  $P_5$ , given shock wave speed, test gas composition, and  $P_1$ , assuming frozen incident and reflected conditions, uncertainties of which are typically within 2% when properly accounting for vibrational relaxation of all components of the test gas [4] [6]. A dynamic pressure transducer (Kistler 601B) was mounted in the end wall of the test section of the HEST, recording pressure traces of the reflected shock

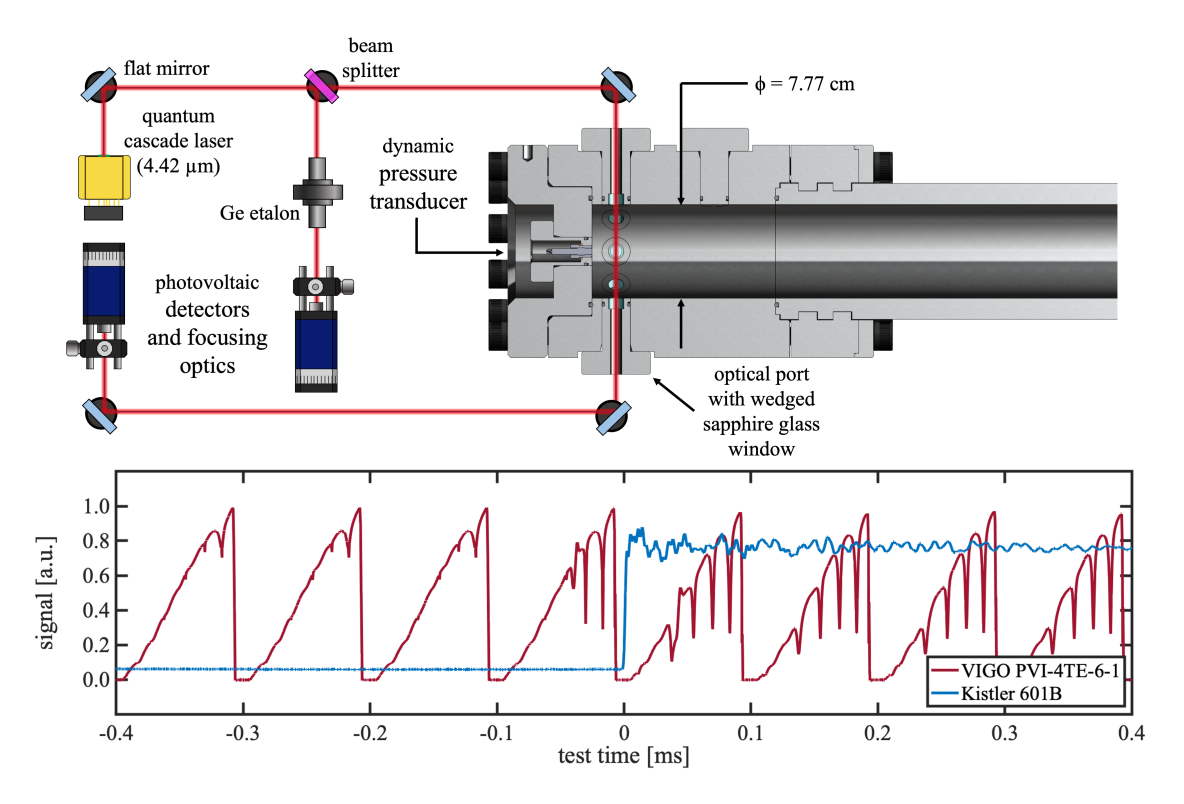


Fig. 3 Top: optical setup for simultaneous measurement of transmitted QCL intensity and incident etalon-influenced QCL intensity on a pair of photovoltaic detectors. Bottom: representative raw detector/pressure transducer signals during shock heating of  $N_2O$  in an Ar bath gas.

wave through a charge amplifier (Kistler 5018A), providing time-resolved validation of CEA assumptions.

## V. Data processing

## A. Broadening parameter determination

Raw detector data, as shown in Figs 3 and 4 were processed using Eq. (1) to obtain spectral absorbance  $\alpha_j(\nu)$  for features R(0,58–61). A non-linear least-squares fitting routine was used to fit all four spectral features simultaneously using a Voigt lineshape model, shown in Fig. 5. For each feature, absorbance area,  $A_j$  and the collisional width,  $\Delta \nu_{c,j}$  were floated as free parameters, while  $\Delta \nu_{D,j}$  were constrained using  $T_5$  as a temperature estimate. Additionally, the R(0,60) feature's linecenter,  $\nu_0$ , was floated as a free parameter, while the other linecenters were constrained based on their relative separation in HITEMP. Residuals were all within 5% during the experiments, confirming the appropriateness of the Voigt lineshape model for the targeted spectral transitions in this study.

To determine the temperature-independent spectral broadening parameter for Ar,  $2\gamma_{N_2O-Ar}(T_0)$  and its associated temperature dependence, N Eq. (6) was used to determine the temperature dependent spectral broadening parameter  $2\gamma_{N_2O-Ar}(T)$  based on  $X_{N_2O}$ , P,  $2\gamma_{self}(T_0)$ , and  $N_{self}$  from the floated variable  $\Delta v_{c,j}$ . To reduce effects of outlier data, Chauvenet's criterion was applied to this and all results [17]. For all calculations,  $N_{self}$  was assumed to have a value of 0.7 [6]. Equation (7) was fit to  $2\gamma_{N_2O-Ar}(T_0)$  and T for eight  $T_5$  (post-shock) and one  $T_1$  (pre-shock) conditions. The regression for the R(0,60) spectral feature is shown in Fig. [5]. Results from this regression are presented in Table [1] along with the spectral parameters (HITEMP) used in this spectral fitting routine and thermochemical analysis via Boltzmann regression. To the authors' knowledge, these data represent the first collection of broadening parameters collected for these  $N_2O$  transitions for the collision partner of argon at elevated temperatures (> 1000 K).

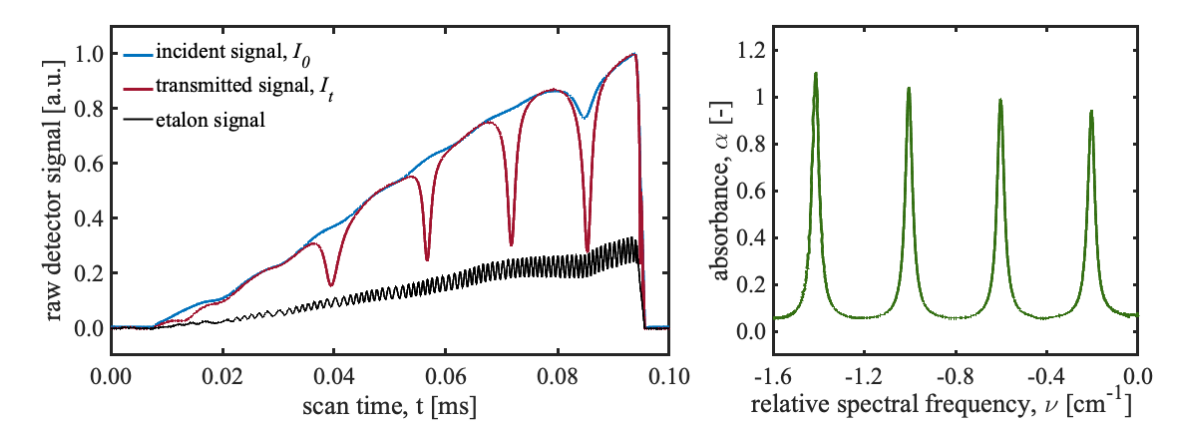


Fig. 4 Plots of incident, transmitted, and etalon-influenced signals on photovoltaic detectors (left) and associated spectral absorbance (right) for a single representative laser scan.

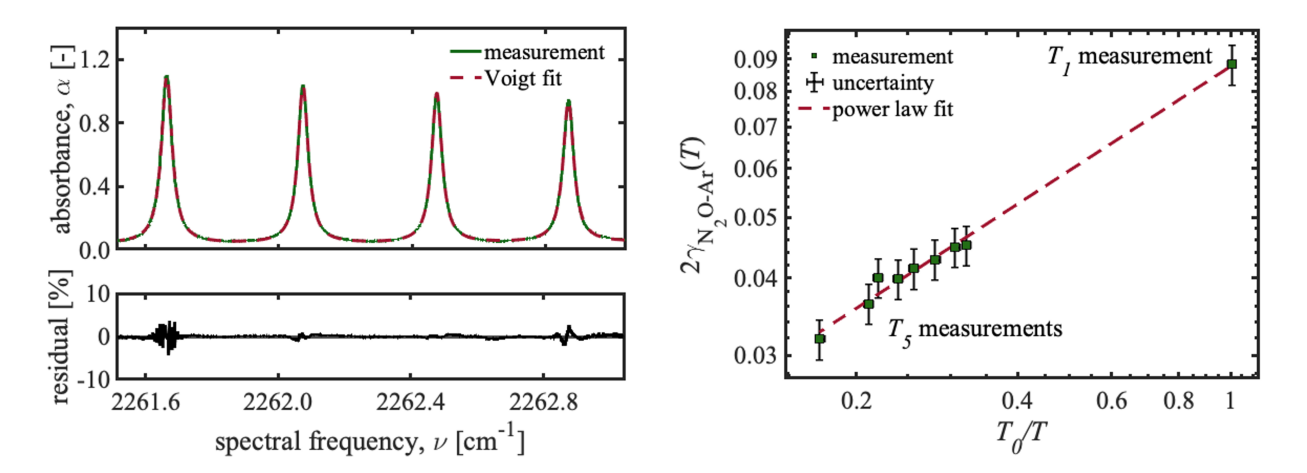


Fig. 5 Left: representative four-feature fit with residual. Right: Power-law regression used to determine  $2\gamma_{N_2O-Ar}(T_0)$  and N for the R(0,60) spectral feature. Here, x-axis uncertainty is plotted although is not visible at this scale.

## B. Reduced parameter spectral fitting

As previously discussed in Sec.  $\overline{\text{V.A}}$  a non-linear least-squares fitting routine was used to fit all four targeted spectral features simultaneously using a Voigt lineshape model, shown in Fig.  $\overline{\textbf{O}}$ . For each feature peak absorbance,  $\alpha_j(\nu_0)$  [unitless] was floated as a free parameter. Additionally, the R(0,60) feature's linecenter,  $\nu_0$  was floated as a free parameter along with temperature, T, while pressure, P ( $P_5$  via NASA CEA), and N<sub>2</sub>O mole fraction, X (assuming no thermal decomposition), were fixed. By allowing T to float as a free parameter and using P and X as inputs along with the determined broadening parameters (e.g.,  $2\gamma_{\text{self}}$ ,  $N_{\text{self}}$ ,  $2\gamma_{\text{N}_2\text{O-Ar}}$ ,  $N_{\text{N}_2\text{O-Ar}}$ ) to the spectral model, collisional and Doppler widths,  $\Delta\nu_C$  and  $\Delta\nu_D$  could vary while the fitting function optimized the spectral fit using Eqs.  $\overline{\textbf{O}}$  and  $\overline{\textbf{O}}$ . After fitting, absorbance areas,  $A_j$ , were determined numerically for use in a Boltzmann regression to determine T and X. As before, residuals were all within 5% during the experiments, confirming the appropriateness of the Voigt lineshape model for this study.

To calculate thermochemical properties T and X, a Boltzmann regression of rovibrational state population fractions was performed using the absorbance areas,  $A_j$ , determined using the reduced parameter spectral fit. In this approach, Eq. (II) was linearized such that:

$$y = \ln \left[ \frac{A_j}{PS_j^0 L} \right] \tag{12}$$

Feature	$\nu_{0,j}$	$E_j^{\prime\prime}$	$S_j^{0*}$		$2\gamma_{\mathrm{N_2O-Ar},j}(T_0)^{\ddagger}$	$N_{\mathrm{N_2O-Ar},j}^{\ddagger}$
R(v'', J'')	[cm <sup>-1</sup> ]	[cm <sup>-1</sup> ]	[cm <sup>-2</sup> atm <sup>-1</sup> ]	[cm <sup>-1</sup> atm <sup>-1</sup> ]	[cm <sup>-1</sup> atm <sup>-1</sup> ]	[unitless]
R(0,58)	2261.262	1481.092	0.1150	0.077	0.111	0.70
R(0,59)	2261.672	1531.221	0.0913	0.077	0.099	0.64
R(0,60)	2262.074	1582.180	0.0725	0.076	0.088	0.56
R(0,61)	2262.470	1633.969	0.0573	0.076	0.088	0.55

<sup>\*</sup>Uncertainty: > 20%

Table 1 Tabulated (HITEMP) and calculated spectroscopic parameters for targeted  $N_2O$  absorption features and associated uncertainties

and

$$x = E_i^{"} \tag{13}$$

before linear regression was performed to determine the slope, a. A representative regression is shown in Fig.  $\boxed{0}$ . From the slope, temperature, T was found found using the equation presented in Fig.  $\boxed{1}$ . Finally, with T known, temperature-dependent linestrength,  $S_j(T)$  was calculated using  $\boxed{10}$ , allowing for the determination of X with Eq.  $\boxed{9}$ , using the absorbance area of the R(0,60) feature.

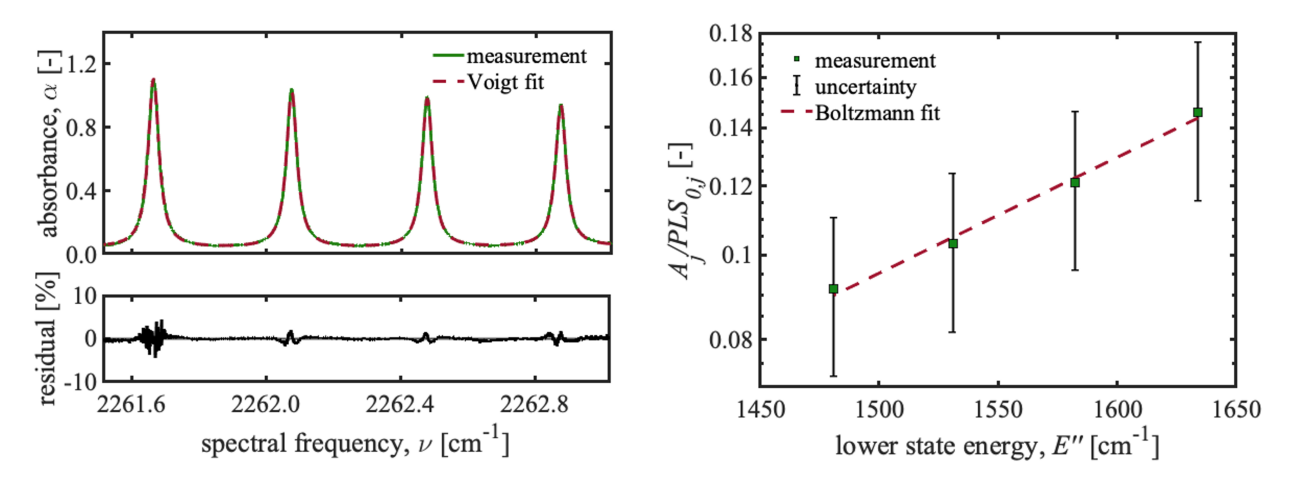


Fig. 6 Left: representative four-feature, reduced parameter fit with residual. Right: Boltzmann regression used to determine temperature, T and  $N_2O$  mole fraction, X.

## VI. Results

In this section, we describe the performance of the sensing technique detailed in the previous sections, starting with a validation of the inferred time-resolved  $N_2O$  temperature and mole fraction results against the known values behind reflected shock waves ranging from 900–1400 K in temperature, and concluding with a time-resolved measurement of  $N_2O$  mole fraction as the species thermally decomposes behind a reflected shock wave at a higher temperature (>1700 K) than the validation tests.

### A. Thermochemical sensor validation results

For shock tube experiments where no thermal decomposition of  $N_2O$  was observed during the test time ( $T \leq 1700 \text{ K}$ ), average temperature and mole fractions were calculated from the methods described previously in Section |V| A

<sup>†</sup>Uncertainty:  $\geq 2\%$  and < 5%‡Uncertainty:  $\geq 5\%$  and < 10%

representative plot of temperature and mole fraction measurement is presented in  $\boxed{7}$  demonstrating the absence of N<sub>2</sub>O thermal decomposition, evident by a constant  $X_{\rm N_2O}$  throughout the test. Here,  $T_5 = 967$  K and  $P_5 = 0.874$  atm. The uncertainties, at present, are conservatively large, and this is discussed in further detail in Section  $\boxed{\rm VII}$  as well as the Appendix. Nonetheless, the nominal values of temperature and mole fraction are observed to be stable over the shock tube test time (approximately 3 ms), with the fixed-parameter calculations yielding more stable values than the Boltzmann-regression-based calculations.

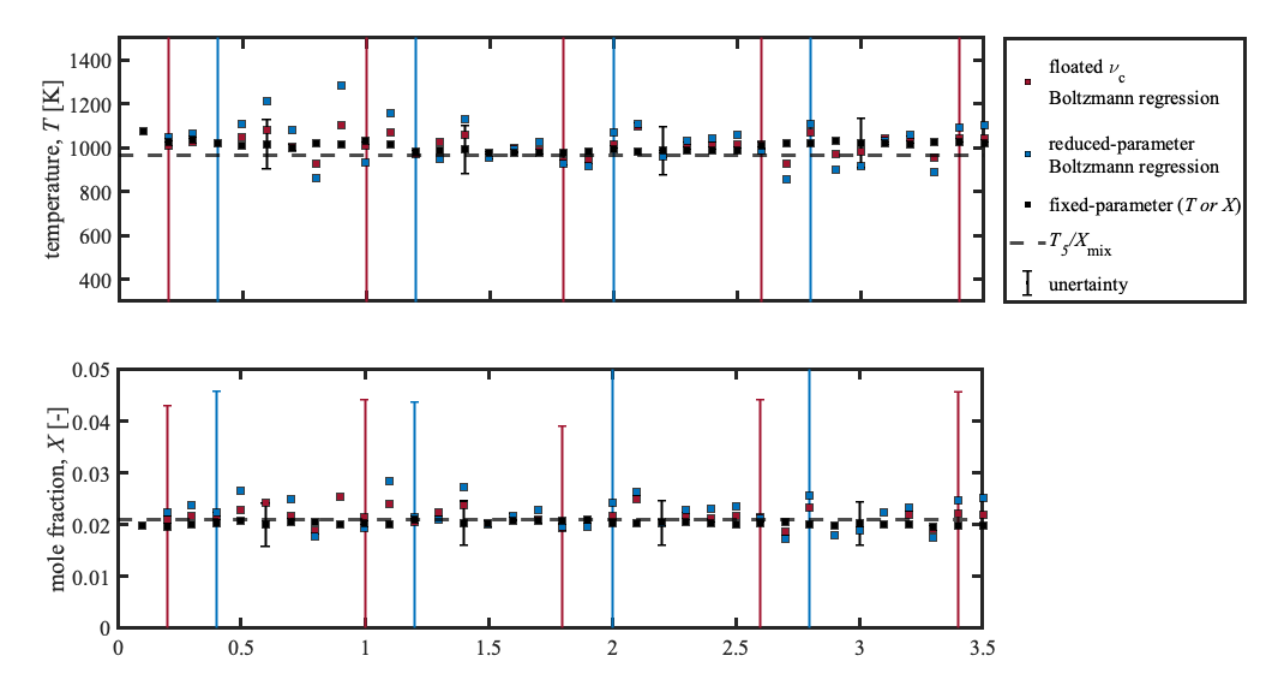


Fig. 7 Measured temperature and mole fraction of  $N_2O$  based on the Boltzmann regression technique described in Section  $\overline{IV}$  as well as the fixed-parameter method described in the same section, with comparison to calculation from the ideal shock relations and known mixture concentrations.

The averaging of this data resulted in 7 measurements of each thermodynamic state variable across a range of  $T_5$  conditions (920–1400 K). Temperatures were measured using three methods: 1) a spectral fitting routine in which absorbance area,  $A_j$  was floated and a Boltzmann regression of rovibrational state population fractions was performed, 2) a reduced-parameter spectral fitting routine where mole fraction was fixed ( $X = X_{\text{mix}}$  and temperature, T was floated, and 3) the reduced-parameter spectral fitting routine was used to determine  $A_j$  and a Boltzmann regression was performed. Additionally,  $N_2O$  mole fractions were determined using a combination of the previously described spectral fitting routines and  $T_5$  with Eq. (9). The results of these approaches are presented in Fig. where T at each  $T_5$  are plotted on the top and  $X_{\text{meas}}/X_{\text{mix}}$  at each  $T_5$  are plotted on the bottom. Uncertainties are plotted for each measurement, whose derivation is discussed in the Appendix. Notably, the uncertainties for the Boltzmann-regression based methods are presently conservatively large, and this is discussed at more length in Section VII.

## B. Time-resolved N<sub>2</sub>O kinetics sensor demonstration

In order to demonstrate the ability of the LAS technique developed in this work to measure  $N_2O$  concentration changing in time, a reflected shock was generated with a sufficiently high temperature to initiate decomposition of  $N_2O$ . Fig.  $\boxed{9}$  shows measured  $N_2O$  mole fraction under reflected shock conditions  $T_5=1733$  K and  $P_5=0.853$  atm for an initial concentration of  $X_{N_2O}=0.02012$ , along with predictions by chemical kinetic models using Cantera  $\boxed{18}$ . For the mole fraction results shown in Fig.  $\boxed{9}$  the temperature is assumed constant at the  $T_5$  value predicted by NASA CEA. Though not entirely representative of the temperature in the shock tube test section (since the decomposition of  $N_2O$  is exothermic), the temperature changes are expected to be small (<100 K) owing to the high dilution (98%) of the mixture.  $X_{N_2O}$  is observed to decrease, dropping to 0.0065 before the end of the test time for the current configuration of

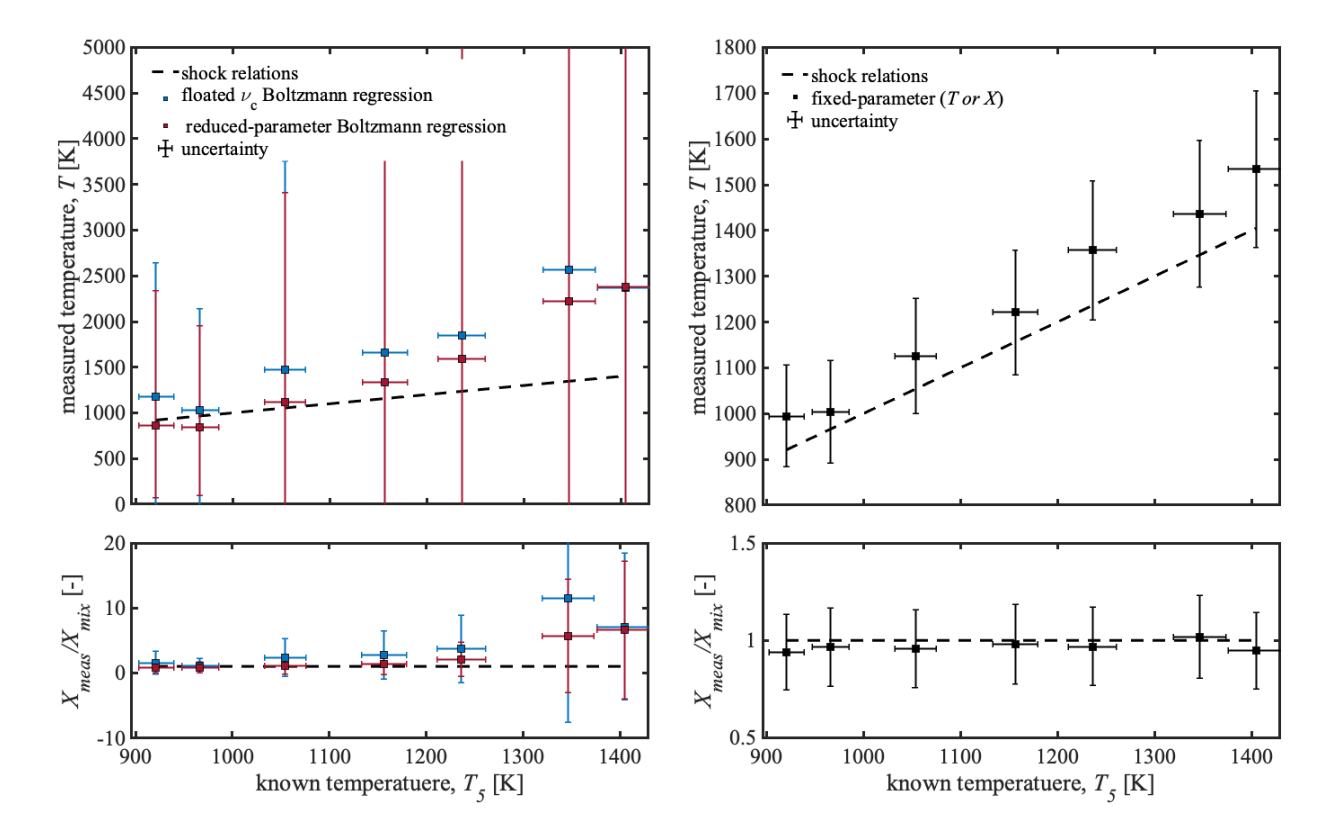


Fig. 8 Left: average T (top) and  $X_{N_2O}$  (bottom) results calculated via Boltzmann regression using two different spectral fitting routines. Right: average T and  $X_{N_2O}$  results calculated using a fitting routine where T was floated (top), and a fitting routine where T was floated and used to calculate T via Eq. (9) (bottom).

the shock tube. The experimental measurements qualitatively agree with model predictions, though the models are observed to substantially under-predict the rate of  $N_2O$  decomposition. This is not unexpected, as neither model has been optimized for  $N_2O$  decomposition. However, recent updated rates measured by Mulvihill et al. [2] are expected to improve the agreement among models and the experiments. This will be explored in future investigations. Nonetheless, the technique is demonstrated to provide experimental time-resolved mole fraction data that can be compared with chemical kinetic models, and may be useful in future efforts to refine them.

## VII. Summary, discussion, and future work

In this study, we described the development and testing of a mid-infrared scanned-wavelength laser absorption spectroscopy sensing technique for time-resolved thermochemical analysis of  $N_2O$  in high-enthalpy, combustion-relevant environments. A quantum cascade laser near 4.4  $\mu$ m was used to scan across a collection of spectral transitions in the  $v_3$  fundamental band of  $N_2O$ , both for the determination of fundamental spectroscopic broadening parameters in an argon bath gas as well as for the quantitative time-resolved measurement of  $N_2O$  temperature and mole fraction from 900–1700 K. To the authors' knowledge, these data represent the first collection of broadening parameters determined for these  $N_2O$  transitions for the collision partner of argon at elevated temperatures (> 1000 K). The use of these newly-measured spectroscopic parameters as additional constraints in our spectral fitting routines was observed to reduce experimental uncertainty and improve agreement with known temperature and mole fraction values.

The deviations from known temperature  $T_5$  from inferred temperature shown in Fig. 8 tend to either increase as known temperature increases (for the Boltzmann regression-based methods) or exhibit a systemic positive bias (for the fixed-parameter-based method), despite constraining the spectral fits with updated broadening parameters obtained in high-temperature shock tube experiments. Notably, these temperatures are inferred using the reference-temperature

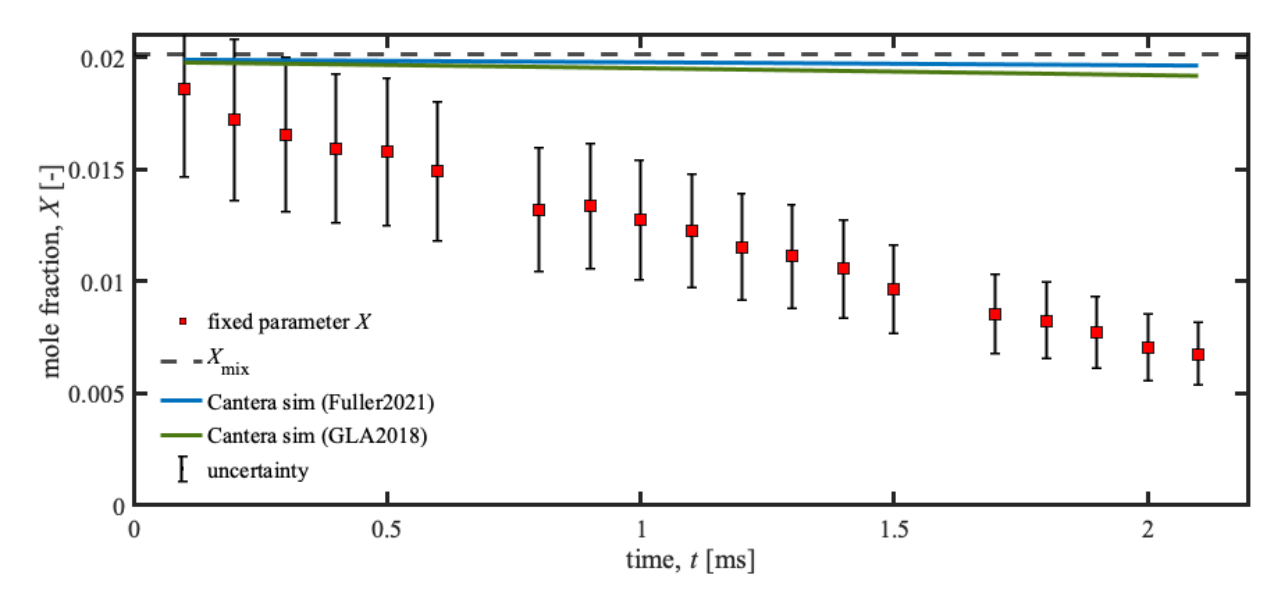


Fig. 9 Time-resolved measurements of  $X_{N_2O}$ , shown to be thermally decomposing at a  $T_5 = 1734$  K. For comparison, mixture mole fraction and time-resolved simulated mole fractions using the Fuller2021 [19] and GLA2018 [20] mechanisms are shown.

linestrength data  $(S_j(T_0))$  available for N<sub>2</sub>O in HITEMP [9], which for the target transitions are documented to have  $\geq 20$  % uncertainty. Although the Boltzmann regression is subject to uncertainty owing the relatively small differences in lower state energy amongst the targeted transitions (as shown in Fig. 6), it is possible that these R(0,58)–R(0,61) transitions—along with others in the same  $v_3$  band—require a revision in their values for reference-temperature linestrengths before they can be used more reliably in kinetics investigations related to storable propellant chemistry and nitrogen-based and hydrogen-carrier energy conversion. For this reason, at present, we recommend caution when using the broadening parameters listed in Table [1], until more refined data can be collected. It is also possible that the assumption of 'frozen' ideal gas conditions in the incident and reflected shock regions of the experiments are not appropriate for mixtures containing 2% N<sub>2</sub>O, and real-gas effects or vibrational relaxation behavior may influence the calculated value of  $T_5$  for the shock tube experiments. Future work will involve a systematic investigation using reflected shocks in the UTSA HEST facility at elevated temperatures to refine and determine the linestrengths and broadening parameters for all N<sub>2</sub>O transitions accessible to the QCL used in this study. It is envisioned that—with updated and refined spectral parameters—the uncertainties in the inferred temperature measurements will tighten, enabling the use of these N<sub>2</sub>O features for sensitive temperature and species measurements in reacting systems relevant to storable propellants and low-carbon energy conversion.

## Appendix

Here, the uncertainties for the collisional broadening parameter,  $2\gamma_{abs-Y}(T_0)$  and its temperature dependence  $N_{abs-Y}$  are discussed following the methods used in [21]. Additionally, following the methods used by [11], the uncertainties for temperature, T (Boltzmann) and mole fraction, X are discussed.

The uncertainty of function f, as a function of variables  $x_i$ , can be calculated using a Taylor expansion, shown in Eq. (14), assuming the measured variables,  $x_i$ , and measured variable uncertainties,  $\delta x_i$ , are independent from one another [17]. Using this, the uncertainty of function f can be expressed as a function of its partial derivatives and independent variable uncertainties, shown in Eq. (15).

$$df(x_1, x_2, \dots) = \frac{\partial f}{\partial x_1} dx_1 + \frac{\partial f}{\partial x_2} dx_2 + \dots$$
 (14)

$$(\delta f)^2 = \left(\frac{\partial f}{\partial x_1} \delta x_1\right)^2 + \left(\frac{\partial f}{\partial x_2} \delta x_2\right)^2 + \dots$$
 (15)

Applying Eq. (15) to Eq. (6) (rearranged to solve for  $2\gamma_{N_2O-Y,j}$ ) yields:

$$\left(\frac{\delta 2\gamma_{\text{abs-Y},j}(T_0)}{2\gamma_{\text{abs-Y},j}(T_0)}\right)^2 = \left(\frac{\delta P}{P}\right)^2 + \left(\frac{\delta X}{X}\right)^2 + \left(\frac{\delta 2\gamma_{\text{self},j}(T_0)}{2\gamma_{\text{self},j}(T_0)}\right)^2 + \left(\frac{\delta \Delta \nu_{c,j}}{\Delta \nu_{c,j}}\right)^2 \tag{16}$$

where the uncertainties in  $P = P_5$  were taken as 2% (NASA CEA), the uncertainties in X were taken to be 0.0015% (based on the partial pressure mixing procedure), the uncertainties in  $2\gamma_{\text{self},j}$  was taken to be 5% (HITEMP), and the uncertainties in  $\Delta\nu_{c,j}$  were taken to be 5% (average maximum residual). Extending this result to Eq. (7) to determine and applying Eq. (15):

$$\left(\frac{N_{\text{abs-Y},j}}{N_{\text{abs-Y},j}}\right)^2 = \left(\frac{\delta T}{T}\right)^2 + \left(\frac{\delta 2\gamma_{\text{abs-Y},j}(T_0)}{2\gamma_{\text{abs-Y},j}(T_0)}\right)^2 \tag{17}$$

where the uncertainty in  $T = T_5$  was taken as 2% (NASA CEA).

Restating the equation for temperature from Fig. []:

$$T = \left[\frac{1}{T_0} - \frac{ak_B}{hc}\right]^{-1} \tag{18}$$

where  $T_0$ ,  $k_B$ , h, and c are constants and a is the slope of the Boltzmann regression. Applying Eq. (15) to Eq. (18) and accounting for uncertainty propagation [22]:

$$\frac{\delta T}{T} = \frac{k_B}{hc} T \delta a \tag{19}$$

where  $\delta a$  is the uncertainty in the slope of the Boltzmann regression. Although this can be expressed as the standard error (95% confidence interval) as in [7], this approach does not specifically account for spectroscopic parameters or signal noise. To account for these terms, an uncertainty analysis of a as a function of  $y = ln\left(\frac{A_j}{PLS_{0,j}}\right)$  is useful.

As previously discussed, the uncertainty in  $A_j$  were taken to be 5% (average maximum residual) while the uncertainties in  $P = P_5$  were taken to be 2% (NASA CEA). The uncertainty in L was taken to be 0.0007% (HEST manufacturing tolerances). The uncertainties in reference linestrength,  $\delta S_j^0$  ere taken to be 20% (HITEMP). Applying Eq. (15) to y leads to:

$$\left(\frac{\delta y}{y}\right)^2 = \left(\frac{\delta A_j}{A_j}\right)^2 + \left(\frac{\delta P}{P}\right)^2 + \left(\frac{\delta L}{L}\right)^2 + \left(\frac{\delta S_j^0}{S_i^0}\right)^2 \tag{20}$$

In determining the uncertainty of the Boltzmann regression slope a, the uncertainty associated with E'' can be neglected as it is on the order of  $10^{-6}$  [11]. Accounting for the effects of multiple lines by using the methods in [22]:

$$\delta a = \frac{1}{\Delta E'' \sqrt{n-1}} \sqrt{\left(\frac{\delta A_j}{A_j}\right)^2 + \left(\frac{\delta P}{P}\right)^2 + \left(\frac{\delta L}{L}\right)^2 + \left(\frac{\delta S_j^0}{S_j^0}\right)^2} \tag{21}$$

where n is the total number of lines in the regression.

Finally, applying Eq. (15) to Eq. (9) yields:

$$\left(\frac{\delta X}{X}\right)^2 = \left(\frac{\delta A_j}{A_j}\right)^2 + \left(\frac{\delta P}{P}\right)^2 + \left(\frac{\delta S_j(T)}{S_j(T)}\right)^2 + \left(\frac{\delta L}{L}\right)^2 \tag{22}$$

As defined in [21], the absolute uncertainty of the temperature dependant linestrength,  $S_{i,T}(T)$  is:

$$\delta S_{j,T}(T)^{2} = S_{j}(T)^{2} \delta T^{2} \left[ -\frac{\partial \mathcal{Z}(T)/\partial T}{\mathcal{Z}(T)} - \frac{1}{T} + \frac{hcE_{j}''}{k_{B}T^{2}} + \frac{hc\nu_{0,j}}{k_{B}T^{2}} \left( \frac{\exp(-hc\nu_{o,j}/k_{B}T)}{1 - \exp(-hc\nu_{o,j}/k_{B}T)} \right) \right]^{2}$$
(23)

being a function of temperature T, where the partial derivative of the partition function  $\mathcal{Z}(T)$  is taken numerically. With this, the absolute uncertainty in  $S_i(T)$  is defined as:

$$\delta S_{i}(T)^{2} = \delta S_{i,T}(T)^{2} + \delta S_{i}(T_{0})^{2}$$
(24)

# Acknowledgments

This study is supported by the U.S. National Science Foundation, Award No. 2135789. BRS and LM are supported in part by the American Chemical Society Petroleum Research Fund (ACS-PRF Grant No. 65560-DNI6), while MBJ and AMF are supported in part by the U.S. National Science Foundation, Award No. 2135789 and 2339502. Student travel associated with the presentation of the work in this study is also partially supported by the U.S. National Aeronautics and Space Administration (NASA) MUREP Institutional Research Opportunity (MIRO) Award, Cooperative Agreement No. 80NSSC19M0194.

This work represents the first spectroscopic data collected in the UTSA HEST Facility, the construction of which was a significant collective effort over multiple years against many manufacturing adversities encountered in the wake of the COVID-19 pandemic. Although much work remains to be done (as always), the authors would like to take this opportunity to thank Joseph G. Hernandez-McCloskey, Kyle L. Fetter, Kevin M. Eisenbarger, Seth Reutlinger, Justin Torbey, Tristan Z. Crumley, Zechariah J. Knowlton, Brandon M. Ng, Krystal Corral Martinez, Kelsey Kettel, Daniella Rivas, M. Grace Zimmer, Madeline M. De La Garza, Makayla A. Watts, Sumona Donde, Isaac Esparza Villarreal, Christopher Y. Ochoa, Micah S. Burton, and Christopher Mendez for their efforts in the design, fabrication, assembly, and testing of the UTSA HEST Facility. The authors are especially grateful to Mr. Dave Kuenstler for his patience, guidance, and assistance to students during the manufacturing of multiple components of the facility.

The authors also would like to thank Prof. Christopher Combs and the UTSA Hypersonics Laboratory for the generous loan of their engine hoist used in the assembly of the UTSA HEST Facility. The efforts of Andrew Alexander, Shelby Franklin, and Carson Bush in the initial development of the HEST data acquisition and control system are also gratefully acknowledged, along with those associated with the initial design review input from Fabio A. Bendana, Anil P. Nair, Nicholas M. Kuenning, Christopher Jelloian, Prof. Don Petersen, and Natalie Metzger.

### References

- [1] Mulvihill, C. R., Alturaifi, S. A., Mathieu, O., and Petersen, E. L., "A N2O laser absorption diagnostic near 4.6 μm for shock-tube chemical kinetics studies," *AIAA Scitech 2020 Forum*, Vol. 1 PartF, No. January, 2020, pp. 1–6. https://doi.org/10.2514/6.2020-2143.
- [2] Mulvihill, C. R., Alturaifi, S. A., and Petersen, E. L., "A shock-tube study of the N2O + M N2 + O + M (M = Ar) rate constant using N2O laser absorption near 4.6 µm," *Combustion and Flame*, Vol. 224, 2021, pp. 6–13. https://doi.org/10.1016/j.combustflame.2020.10.040, URL https://doi.org/10.1016/j.combustflame.2020.10.040
- [3] Alturaifi, S. A., Mathieu, O., and Petersen, E. L., "Shock-tube laser absorption measurements of N2O time histories during ammonia oxidation," *Fuel Communications*, Vol. 10, No. October 2021, 2022, p. 100050. https://doi.org/10.1016/j.jfueco.2022.100050, URL https://doi.org/10.1016/j.jfueco.2022.100050.
- [4] Anderson, J. D., Modern Compressible Flow, A Historical Perspective, 3<sup>rd</sup> ed., McGraw-Hill, New York, NY, 2002.
- [5] Hernandez-McCloskey, J., Steavenson, B. R., Pineda, D. I., Alexander, A., Franklin, S., and Bush, C., "Design of the UTSA High-Enthalpy Shock Tube Facility," AIAA Scitech 2023 Forum Forum, , No. January, 2023, pp. 1–11. https://doi.org/10.2514/6.2023-0018
- [6] Hanson, R. K., Spearrin, R. M., and Goldenstein, C. S., Spectroscopy and optical diagnostics for gases, 1<sup>st</sup> ed., Springer, London, UK, 2016. https://doi.org/10.1007/9783319232522.
- [7] Steavenson, B., Munera, L., Crumley, T. Z., Guerra, D. Y., Corral-Martinez, K., and Pineda, D. I., "Mid-infrared N2O absorption sensor for high-enthalpy flows relevant to hypersonic ground testing," *AIAA SCITECH 2024 Forum*, American Institute of Aeronautics and Astronautics, Reston, Virginia, 2024, pp. 1–15. <a href="https://doi.org/10.2514/6.2024-2496">https://doi.org/10.2514/6.2024-2496</a>, URL <a href="https://arc.aiaa.org/doi/10.2514/6.2024-2496">https://arc.aiaa.org/doi/10.2514/6.2024-2496</a>.
- [8] Steavenson, B., Hernandez-McCloskey, J., and Pineda, D. I., "Thermodynamic analysis of nitric oxide in an optically accessible, temperature-controlled gas cell via laser absorption spectroscopy," AIAA Scitech 2023 Forum Forum, No. January, 2023, pp. 1–11. <a href="https://doi.org/10.2514/6.2023-0011">https://doi.org/10.2514/6.2023-0011</a>.
- [9] Rothman, L. S., Gordon, I. E., Barber, R. J., Dothe, H., Gamache, R. R., Goldman, A., Perevalov, V. I., Tashkun, S. A., and Tennyson, J., "HITEMP, the high-temperature molecular spectroscopic database," *Journal of Quantitative Spectroscopy and Radiative Transfer*, Vol. 111, No. 15, 2010, pp. 2139–2150. https://doi.org/10.1016/j.jqsrt.2010.05.001, URL http://dx.doi.org/10.1016/j.jqsrt.2010.05.001.

- [10] Gordon, I., Rothman, L., Hargreaves, R., Hashemi, R., Karlovets, E., Skinner, F., Conway, E., Hill, C., Kochanov, R., Tan, Y., Wcisło, P., Finenko, A., Nelson, K., Bernath, P., Birk, M., Boudon, V., Campargue, A., Chance, K., Coustenis, A., Drouin, B., Flaud, J., Gamache, R., Hodges, J., Jacquemart, D., Mlawer, E., Nikitin, A., Perevalov, V., Rotger, M., Tennyson, J., Toon, G., Tran, H., Tyuterev, V., Adkins, E., Baker, A., Barbe, A., Canè, E., Császár, A., Dudaryonok, A., Egorov, O., Fleisher, A., Fleurbaey, H., Foltynowicz, A., Furtenbacher, T., Harrison, J., Hartmann, J., Horneman, V., Huang, X., Karman, T., Karns, J., Kassi, S., Kleiner, I., Kofman, V., Kwabia–Tchana, F., Lavrentieva, N., Lee, T., Long, D., Lukashevskaya, A., Lyulin, O., Makhnev, V., Matt, W., Massie, S., Melosso, M., Mikhailenko, S., Mondelain, D., Müller, H., Naumenko, O., Perrin, A., Polyansky, O., Raddaoui, E., Raston, P., Reed, Z., Rey, M., Richard, C., Tóbiás, R., Sadiek, I., Schwenke, D., Starikova, E., Sung, K., Tamassia, F., Tashkun, S., Vander Auwera, J., Vasilenko, I., Vigasin, A., Villanueva, G., Vispoel, B., Wagner, G., Yachmenev, A., and Yurchenko, S., "The HITRAN2020 molecular spectroscopic database," *Journal of Quantitative Spectroscopy and Radiative Transfer*, Vol. 277, 2022, p. 107949. https://doi.org/10.1016/j.jqsrt.2021.107949.
- [11] Minesi, N. Q., Richmond, M. O., Jelloian, C. C., Kuenning, N. M., Nair, A. P., and Spearrin, R. M., "Multi-line Boltzmann regression for near-electronvolt temperature and CO sensing via MHz-rate infrared laser absorption spectroscopy," *Applied Physics B: Lasers and Optics*, Vol. 128, No. 12, 2022, pp. 1–17. <a href="https://doi.org/10.1007/s00340-022-07931-7">https://doi.org/10.1007/s00340-022-07931-7</a>. URL <a href="https://doi.org/10.1007/s00340-022-07931-7">https://doi.org/10.1007/s00340-022-07931-7</a>.
- [12] Pathria, R., and Beale, P., Statistical mechanics, 4th ed., Elsevier, London, UK, 2022.
- [13] Girard, J. J., Spearrin, R. M., Goldenstein, C. S., and Hanson, R. K., "Compact optical probe for flame temperature and carbon dioxide using interband cascade laser absorption near 4.2µm," *Combustion and Flame*, Vol. 178, 2017, pp. 158–167. https://doi.org/10.1016/j.combustflame.2017.01.007 URL http://dx.doi.org/10.1016/j.combustflame.2017.01.007
- [14] Nair, A. P., Minesi, N. Q., Jelloian, C., Kuenning, N. M., and Spearrin, R. M., "Extended tuning of distributed-feedback lasers in a bias-tee circuit via waveform optimization for MHz-rate absorption spectroscopy," *Measurement Science and Technology*, Vol. 33, No. 10, 2022. https://doi.org/10.1088/1361-6501/ac7b13
- [15] Gordon, R. G., and McGinnis, R. P., "Line Shapes in Molecular Spectra," The Journal of Chemical Physics, Vol. 49, No. 5, 1968, pp. 2455–2456. https://doi.org/10.1063/1.1670429.
- [16] Campbell, M. F., Owen, K. G., Davidson, D. F., and Hanson, R. K., "Dependence of Calculated Postshock Thermodynamic Variables on Vibrational Equilibrium and Input Uncertainty," *Journal of Thermophysics and Heat Transfer*, Vol. 31, No. 3, 2017, pp. 586–608. https://doi.org/10.2514/1.T4952.
- [17] Chapra, S., and Canale, R., Numerical Methods for Engineers, 7th ed., November, McGraw-Hill, New York, NY, 2015.
- [18] Goodwin, D. G., Moffat, H. K., and Speth, R. L., "Cantera: An object-oriented software toolkit for chemical kinetics, thermodynamics, and transport processes,", 2018. https://doi.org/10.5281/zenodo.170284.
- [19] Fuller, M. E., Morsch, P., Preußker, M., Goldsmith, C. F., and Heufer, K. A., "The impact of NOxaddition on the ignition behaviour of n -pentane," *Reaction Chemistry and Engineering*, Vol. 6, No. 11, 2021, pp. 2191–2203. https://doi.org/10.1039/d1re00055a.
- [20] Glarborg, P., Miller, J. A., Ruscic, B., and Klippenstein, S. J., "Modeling nitrogen chemistry in combustion," *Progress in Energy and Combustion Science*, Vol. 67, 2018, pp. 31–68. https://doi.org/10.1016/j.pecs.2018.01.002, URL https://doi.org/10.1016/j.pecs.2018.01.002.
- [21] Pineda, D. I., Bendana, F. A., Schwarm, K. K., and Spearrin, R. M., "Multi-isotopologue laser absorption spectroscopy of carbon monoxide for high-temperature chemical kinetic studies of fuel mixtures," *Combustion and Flame*, Vol. 207, 2019, pp. 379–390. https://doi.org/10.1016/j.combustflame.2019.05.030
- [22] York, D., Evensen, N. M., Martinez, M. L., and De Basabe Delgado, J., "Unified equations for the slope, intercept, and standard errors of the best straight line," *American Journal of Physics*, Vol. 72, No. 3, 2004, pp. 367–375. <a href="https://doi.org/10.1119/1.1632486">https://doi.org/10.1119/1.1632486</a>.